Available online at www.sciencedirect.com
ScienceDirect
Journal of Computational Physics 223 (2007) 898–922
JOURNAL OF COMPUTATIONAL PHYSICS
www.elsevier.com/locate/jcp

A high-order photon Monte Carlo method for radiative transfer in direct numerical simulation

Y. Wu, M.F. Modest, D.C. Haworth *

Department of Mechanical and Nuclear Engineering, The Pennsylvania State University, 130 Research Building E, University Park, PA 16802, USA

Received 22 June 2005; received in revised form 3 October 2006; accepted 5 October 2006
Available online 22 November 2006

Abstract

A high-order photon Monte Carlo method is developed to solve the radiative transfer equation. The statistical and discretization errors of the computed radiative heat flux and radiation source term are isolated and quantified. Up to sixth-order spatial accuracy is demonstrated for the radiative heat flux, and up to fourth-order accuracy for the radiation source term. This demonstrates the compatibility of the method with high-fidelity direct numerical simulation (DNS) for chemically reacting flows. The method is applied to address radiative heat transfer in a one-dimensional laminar premixed flame and a statistically one-dimensional turbulent premixed flame. Modifications of the flame structure with radiation are noted in both cases, and the effects of turbulence/radiation interactions on the local reaction zone structure are revealed for the turbulent flame. Computational issues in using a photon Monte Carlo method for DNS of turbulent reacting flows are discussed.

Keywords: Radiation heat transfer; Photon Monte Carlo method; Direct numerical simulation; Chemically reacting flows

1. Introduction

Thermal radiation is an important mode of heat transfer in many combustion systems [1]. Numerical studies of laminar premixed gas flames [2] have shown that reabsorption of emitted radiation can increase burning velocities and extend flammability limits considerably, and fundamental extinction limits independent of the system dimensions can exist due to radiative heat loss. In turbulent combustion, turbulence, chemical kinetics, and radiation are coupled in highly nonlinear ways, leading to entirely new classes of interactions. In much the same way as convection is aided by turbulence, so is radiation, which, in the presence of chemical reactions, may increase several fold due to turbulence interactions.

The importance of the interactions between turbulence and thermal radiation (turbulence–radiation interaction – TRI) has long been recognized [3–8]. TRI arises from highly nonlinear coupling between temperature

* Corresponding author. Tel.: +1 814 863 6269; fax: +1 814 865 3389.
E-mail addresses: dch12@psu.edu (D.C. Haworth).

0021-9991/$ - see front matter
doi:10.1016/j.jcp.2006.10.014

and composition fluctuations in both nonreacting and reacting turbulent flows. In this respect, TRI is akin to the turbulence–chemistry interaction [9] that has been the subject of intense research for many years. Preliminary and state-of-the-art calculations have shown that TRI always increases the heat loss from a flame, and that this additional heat loss can reach 60% of the total and more, leading to a reduction in the local gas temperature of 200 °C or more and, consequently, to significant changes in key pollutant species (particularly NOx and soot) in both luminous and nonluminous turbulent flames (e.g., [6,8,10–18]). Therefore, in many turbulent flames accurate prediction of radiation and TRI can be expected to be at least as important as accurate modeling of combustion rates and turbulence–chemistry interaction. TRI modeling, however, has largely been ignored to date. The difficulty arises from the requirement to capture the interactions between the fluctuating local absorption coefficient κ and the radiative intensity I, and between κ and the Planck function I_b. Traditional moment methods and one-point probability density function (PDF) methods result in many unclosed terms and, consequently, many additional partial differential equations need to be modeled and solved simultaneously, which leads to an important numerical cost [13]. This, together with the fact that accurate radiation modeling even in the absence of TRI is a daunting task, has prompted the majority of researchers to use simplistic radiation models and/or radiation calculations. For example, the widely adopted optically thin-eddy model assumes turbulent eddies to be optically thin and the fluctuations of κ (a local quantity) and the intensity I (a nonlocal quantity) to be uncorrelated. As a result, $\langle \kappa I \rangle \simeq \langle \kappa \rangle \langle I \rangle$, and the knowledge of intensity fluctuations is not required. Here angled brackets $\langle \cdot \rangle$ denote mean quantities and a prime' denotes a fluctuation about the local mean: e.g., $\kappa = \langle \kappa \rangle + \kappa'$. On the other hand, I_b is a function only of local temperature, and the correlation $\langle \kappa I_b \rangle$ can be obtained from a one-point PDF formulation without modeling. TRI effects thus can be approximated using a one-point PDF method together with the optically thin-eddy approximation. The optically thin-eddy model, however, cannot be applied to sooting flames that have optically thick eddies. It may also fail for flows involving molecular gases: the spectrally averaged absorption coefficient of a gas tends to be small, but the absorption coefficient at spectral line centers can be many thousand $\mathrm{cm}^{-1}\,\mathrm{atm}^{-1}$, leading to significant nonzero values of $\langle \kappa' I' \rangle$.

To establish the conditions for which the correlation between κ and I needs to be considered in turbulent combustion and to provide benchmarks for an optically thick-eddy model to be developed for PDF simulations, turbulent chemically reacting flows can be simulated accurately using direct numerical simulation (DNS) [20–22]. The radiation source term in the energy equation is a function of radiative intensity, which is governed by the radiative transfer equation (RTE). DNS of turbulent flames with radiation thus requires solutions to the RTE in addition to the equations of mass, momentum, energy, and species mass fractions. In the present work, a photon Monte Carlo method is developed for the solution of the RTE for the following reasons. First, the computational cost for a photon Monte Carlo method increases roughly linearly with the complexity of the problem. Thus while simple radiation properties and geometry are considered in this method-formulation paper, the approach is particularly well-suited for problems that involve direction- and/or wavenumber-dependent properties and anisotropic scattering and/or for complex geometry. Second, a photon Monte Carlo method theoretically can provide an "exact" solution to the RTE that is compatible with the philosophy of DNS. Alternative methods, such as spherical harmonics and discrete ordinates methods, invoke approximations [1], and may prove to be computationally more expensive to achieve the level of accuracy that is required for DNS (i.e., high-order resolution of directional and spectral variations). A high-order photon Monte Carlo method also would be applicable to large-eddy simulation (LES), although in that case additional modeling would be required for subfilter-scale TRI.

Monte Carlo methods have been applied to a variety of physical problems. General reviews can be found in [23,24]. An example of a photon Monte Carlo method for thermal radiation and TRI in a sooting turbulent flame can be found in [17]. There each optical path was treated as a combination of nonoverlapping multiple segments, each of which may cross multiple computational cells. The radiative properties of the medium along each segment were assumed to be uniform, rendering the method first-order accurate in space. The goal of the present work is to develop a high-order photon Monte Carlo scheme that is compatible with DNS of chemically reacting turbulent flows. The governing equations and physical models are outlined in Section 2. Section 3 describes key elements of the photon Monte Carlo method and the related random number relations. In Section 4 the high-order implementation of the photon Monte Carlo method is developed, and numerical test cases are presented in Section 5. Conclusions and future work are summarized in the final section.

2. Governing equations and physical models

A turbulent, compressible, chemically reacting, radiatively participating ideal-gas mixture is considered. For present purposes, chemical kinetics are represented by a one-step, irreversible, Arrhenius reaction involving two species (reactant and product),

$$R(reactant) \rightarrow P(product).$$

The chemical reaction rate $\dot{w}$ is expressed as

$$\dot{w} = \frac{\dot{w}_R}{Y_{R1}} = \Lambda \rho \widetilde{Y} \exp\left(\frac{-\beta(1-\Theta)}{1-\alpha(1-\Theta)}\right). \tag{1}$$

Here Θ is the reduced temperature, $\Theta = (T - T_1)/(T_2 - T_1)$, where subscript '1' refers to the fresh gases and '2' to the burnt products (T_2 is the adiabatic flame temperature). $\widetilde{Y} = Y_R/Y_{R1}$ is the mass fraction of reactant normalized by the initial mass fraction of reactant, Y_{R1}. The coefficients Λ, α, and β are the reduced preexponential factor, the temperature factor, and the reduced activation energy, respectively,

$$\Lambda = B\exp(-\beta/\alpha), \quad \alpha = (T_2 - T_1)/T_2, \quad \beta = \alpha T_a/T_2,$$

where B is the preexponential factor and T_a is the activation temperature. Detailed kinetics are readily accommodated, where appropriate.

The continuity, momentum, chemical species, and energy equations have the same form as in [19], with the addition of a thermal radiation source term in the energy equation. Thus,

$$\frac{\partial \rho e_t}{\partial t} + \nabla \cdot (\rho e_t + p)\vec{u} = \frac{\partial (u_i \tau_{ij})}{\partial x_j} + \nabla \cdot (\lambda \nabla T) + Q\dot{w} - \nabla \cdot \vec{q}_{\mathrm{rad}}, \tag{2}$$

where ρ, p, T, λ, $\vec{u}$, and $\vec{q}_{\mathrm{rad}}$ are the fluid mass density, thermodynamic pressure, temperature, thermal conductivity, velocity vector, and radiative heat flux vector, respectively. Q is the heat of reaction per unit mass of fresh mixture, $Q = -\Delta h_f^0 Y_{R1}$, where Δh_f^0 is the heat of reaction per unit mass of reactant. τ_{ij} are the components of the viscous stress tensor, and ρe_t is the total energy density per unit volume,

$$\tau_{ij} = \mu\left(\frac{\partial u_i}{\partial x_j} + \frac{\partial u_j}{\partial x_i} - \frac{2}{3}\delta_{ij}\frac{\partial u_k}{\partial x_k}\right),$$
$$\rho e_t = \rho \vec{u} \cdot \vec{u}/2 + p/(\gamma - 1),$$

where μ and γ are the fluid dynamic viscosity and the (constant) ratio of specific heats, respectively.

The radiation source term in Eq. (2) is

$$\nabla \cdot \vec{q}_{\mathrm{rad}} = \int_0^\infty \kappa_\eta \left(4\pi I_{b\eta} - \int_{4\pi} I_\eta \, \mathrm{d}\Omega\right) \mathrm{d}\eta = 4\kappa_P \sigma T^4 - \int_0^\infty \int_{4\pi} \kappa_\eta I_\eta \, \mathrm{d}\Omega \, \mathrm{d}\eta, \tag{3}$$

where

$$\kappa_P \equiv \frac{\int_0^\infty \kappa_\eta I_{b\eta} \, \mathrm{d}\eta}{\int_0^\infty I_{b\eta} \, \mathrm{d}\eta} = \frac{\pi}{\sigma T^4} \int_0^\infty \kappa_\eta I_{b\eta} \, \mathrm{d}\eta \tag{4}$$

is the Planck-mean absorption coefficient. Here σ is the Stefan–Boltzmann constant, η denotes wavenumber, Ω is solid angle, κ_η is the spectral absorption coefficient, $I_{b\eta}$ is the Planck function (a known function of local temperature and wavenumber), and I_η is the spectral radiative intensity. In general, $\kappa_P = \kappa_P(\underline{Y}, T, p)$, where $\underline{Y}$ denotes the vector of species mass fractions. For an absorbing, emitting, and scattering ("radiatively participating") medium, I_η is determined from the radiative transfer equation (RTE) [1]:

$$\frac{\mathrm{d}I_\eta}{\mathrm{d}s} = \hat{s} \cdot \nabla I_\eta = \kappa_\eta I_{b\eta} - \beta_\eta I_\eta + \frac{\sigma_{s\eta}}{4\pi} \int_{4\pi} I_\eta(\hat{s}_i) \Phi_\eta(\hat{s}_i, \hat{s}) \, \mathrm{d}\Omega_i. \tag{5}$$

Here $\hat{s}$ and $\hat{s}_i$ denote unit direction vectors, $\sigma_{s\eta}$ is the spectral scattering coefficient, and $\beta_\eta = \kappa_\eta + \sigma_{s\eta}$ is the spectral extinction coefficient. $\Phi_\eta(\hat{s}_i, \hat{s})$ is the scattering phase function, which describes the probability that

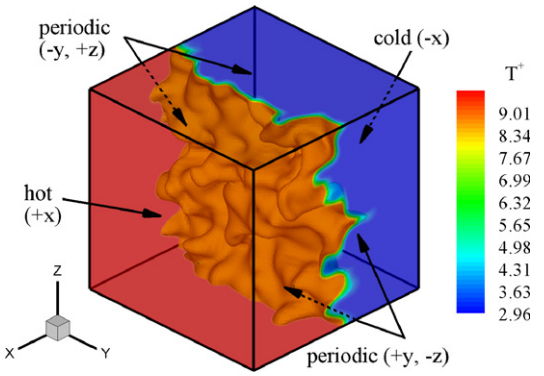

Fig. 1. A statistically one-dimensional turbulent premixed flame. Instantaneous temperature isosurfaces indicate the location of the flame. The figure corresponds to a case with $l_T/l_l = 5.97$ and $u'/s_l = 1.26$, where l_T and u' are the characteristic length and velocity scales of energy-containing turbulent motions, respectively, and l_l and s_l are the thickness and speed of a steady unstrained laminar flame for these thermochemical conditions.

a ray from incident direction $\hat{s}_i$ is scattered into direction $\hat{s}$. The local value of I_η depends on nonlocal properties, on direction $(\hat{s})$, and on wavenumber (η).

In the present work dimensionless forms of the governing equations are solved [19,25]. Nondimensionalization of the new radiation source term in Eq. (2) is given in Appendix A. DNS of chemically reacting turbulent flows requires that all relevant scales be fully resolved with no turbulence models employed. Consequently, high-order numerical schemes and fine grids are required for DNS. Here temporal integration is performed with a Runge–Kutta method of order three; for spatial discretization, a compact finite-difference scheme of order six is used in the interior of the computational domain with various noncentered schemes near boundaries [26]. Temporal discretization is not relevant for the form of the RTE that is considered here (Eq. (5)) and, in general, it is expected that the spatial discretization accuracy required for the RTE need not be as high as that for the hydrodynamics equations. The nonlocal nature of I_η gives a spatial-averaging character to the radiation source term. Still, it is of interest to explore the feasibility of high-order schemes and to use the highest order that is practicable. Here schemes having formal spatial accuracy of up to sixth order for $\vec{q}_{\text{rad}}$ and up to fourth order for $\nabla \cdot \vec{q}_{\text{rad}}$ are developed and tested.

Canonical configurations are considered in DNS studies. For example, Fig. 1 shows a statistically one-dimensional, turbulent premixed flame propagating in the $-x$-direction. There fresh reactants enter the domain from the $-x$ side and burned products leave from the $+x$ side. Two types of flow boundary conditions are considered. Periodic conditions are enforced in the y and z-directions while nonperiodic conditions are enforced in the x-direction using the Navier–Stokes Characteristics Boundary Condition method [27]. Details of the equations, normalizations, and numerical methods (in the absence of thermal radiation) can be found in Ref. [25]. The radiation source term in Eq. (2) is obtained by solving Eq. (5) using the photon Monte Carlo method that is developed herein. Three types of radiation boundary conditions are considered: periodic, cold, and hot boundaries. Their implementation will be explained in subsequent sections.

3. Photon Monte Carlo method for the solution of the RTE

A photon Monte Carlo method solves the RTE by following the trajectories of a large number of representative photon bundles generated using statistical sampling techniques. It consists of two principal parts: an emission stage and a tracing/absorption/scattering stage. Additional considerations are required at boundaries of the computational domain. Emission, tracing/absorption/scattering, and boundary conditions are described in the following three subsections, respectively. These essentially follow the approaches outlined in Chapter 20 of Modest's book [1]. The high-order implementation is developed in Section 4.

3.1. Emission

We define L_x, L_y and L_z as the lengths of a computational domain in the x, y and z-directions, respectively. The total emitted radiant energy from within the domain, E_V, then is

$$E_V = \int_V 4\kappa_P \sigma T^4 \, \mathrm{d}V = \int_0^{L_x} \int_0^{L_y} \int_0^{L_z} 4\kappa_P \sigma T^4 \, \mathrm{d}z \, \mathrm{d}y \, \mathrm{d}x. \tag{6}$$

Each photon bundle represents a specified fraction of E_V and is characterized by six quantities: an emission location (three spatial coordinates for volume emission, two for surface emission), an emission direction (azimuthal angle ψ, polar angle θ), and a spectral variable (wavenumber η). All of these properties need to be determined at the emission stage based on the probabilities of events in the reacting gas mixture. For example, to find the emission location of a photon bundle, the cumulative distribution functions (CDF's) of emission along the x, y, and z-directions are first calculated sequentially as [1],

$$\begin{aligned} R_x &= \frac{\int_0^x \int_0^{L_y} \int_0^{L_z} 4\kappa_P \sigma T^4 \, \mathrm{d}z \, \mathrm{d}y \, \mathrm{d}x}{E_V}, \\ R_y &= \frac{\int_0^y \int_0^{L_z} 4\kappa_P \sigma T^4 \, \mathrm{d}z \, \mathrm{d}y}{\int_0^{L_y} \int_0^{L_z} 4\kappa_P \sigma T^4 \, \mathrm{d}z \, \mathrm{d}y}, \\ R_z &= \frac{\int_0^z 4\kappa_P \sigma T^4 \, \mathrm{d}z}{\int_0^{L_z} 4\kappa_P \sigma T^4 \, \mathrm{d}z}, \end{aligned} \tag{7}$$

where κ_P at each grid point is a function of local temperature, pressure, and species composition and, therefore, is known for a given flowfield. Inversion of Eq. (7) yields the emission position with R_x, R_y, and R_z each sampled independently from a uniform distribution on $[0,1]$: $x = x(R_x)$, $y = y\ (R_y, x)$, $z = z(R_z, x, y)$. Implementation details will be given in Section 4.1.

With the emission position determined, the emission wavenumber is found from the following random number relation:

$$R_\eta = \frac{\pi}{\kappa_P \sigma T^4} \int_0^\eta \kappa_\eta I_{b\eta} \, \mathrm{d}\eta, \tag{8}$$

where R_η is the CDF of the emission wavenumber. After inversion with R_η sampled from a uniform distribution on $[0,1]$, the emission wavenumber is $\eta = \eta(R_\eta, x, y, z)$.

The emission direction is determined in a similar manner. Assuming local thermodynamic equilibrium within the volume, the emission is isotropic; i.e., all possible directions are equally likely for the emission of a photon bundle, and the random number relations for the emission direction are [1]

$$R_\psi = \frac{\psi}{2\pi}, \quad R_\theta = \frac{1}{2}(1 - \cos\theta), \tag{9}$$

where R_ψ and R_θ are the CDF's of azimuthal angle ψ and polar angle θ at emission position (x, y, z), respectively. Inversion of Eq. (9) leads to $\psi = \psi(R_\psi)$ and $\theta = \theta(R_\theta)$.

3.2. Tracing, absorption, and scattering

When radiative energy travels through a participating medium, it is attenuated by absorption and scattered. At the photon tracing stage an energy partitioning scheme [1] is adopted, where the energy of each photon bundle is gradually attenuated due to absorption until: (1) the bundle leaves the enclosure or hits a wall and is absorbed; or (2) its energy is depleted. Mathematically, a photon bundle of initial energy E_0 traveling through a layer of thickness S emerges with radiant energy

$$E_S = E_0 \exp(-\tau_\eta), \tag{10}$$

where $\tau_\eta = \int_0^S \kappa_\eta \, \mathrm{d}s$ is the optical thickness at the wavenumber of the photon bundle. The amount of energy absorbed by the medium is then

$$\triangle E_{\text{abs}} = E_0 - E_S = E_0[1 - \exp(-\tau_\eta)]. \tag{11}$$

Attenuation by scattering obeys the same relationship as for absorption, with the absorption coefficient replaced by the scattering coefficient. Thus, the distance that a photon bundle travels before being scattered can be obtained by inverting the equation:

$$R_\sigma = \exp\left(-\int_0^S \sigma_{s\eta}\,\mathrm{d}s\right), \tag{12}$$

where R_σ is a random number distributed uniformly on $[0,1]$. Once a photon bundle is scattered, it continues to travel in a new direction, where the CDF's of the new azimuthal and polar angles are

$$\begin{aligned} R_{\psi_i} &= \frac{\int_0^{\psi_i}\int_0^{\pi} \Phi(\hat{s},\hat{s}_i)\sin\theta_i\,\mathrm{d}\theta_i\,\mathrm{d}\psi_i}{4\pi}, \\ R_{\theta_i} &= \frac{\int_0^{\theta_i} \Phi(\hat{s},\hat{s}_i)\sin\theta_i\,\mathrm{d}\theta_i}{\int_0^{\pi} \Phi(\hat{s},\hat{s}_i)\sin\theta_i\,\mathrm{d}\theta_i}. \end{aligned} \tag{13}$$

Here $\hat{s}$ is the original direction, and the new polar angle θ_i and azimuthal angle ψ_i are measured from the axis pointing into the $\hat{s}$ direction and in a plane normal to $\hat{s}$, respectively. When scattering is isotropic, the above relations reduce to Eq. (9).

3.3. Boundary conditions

Two types of radiation boundary conditions are considered: periodic and radiative surface conditions. When a photon bundle reaches a radiatively periodic boundary, it re-enters the computational domain at the corresponding point on the opposite side with no change in properties. A radiative surface is a boundary that may emit radiative energy and may partially absorb, partially transmit, and partially reflect radiative energy impinging on it. It can be either a physical boundary or an artificial closing boundary.

Emission from a radiative surface is considered using a two-dimensional analog of Eqs. (7)–(9). Consider the statistically one-dimensional flame shown in Fig. 1 as an example. There an artificial closing surface at the $+x$ (hot) boundary is required with emission from that surface. The emission position of a photon bundle leaving that surface is determined by inversion of the following random number relations:

$$\begin{aligned} R_y &= \frac{\int_0^{y}\int_0^{L_z} \epsilon\sigma T^4\,\mathrm{d}z\,\mathrm{d}y}{E_A}, \\ R_z &= \frac{\int_0^{z} \epsilon\sigma T^4\,\mathrm{d}z}{\int_0^{L_z} \epsilon\sigma T^4\,\mathrm{d}z}. \end{aligned} \tag{14}$$

Here ϵ is the total hemispherical emittance of the surface and E_A is the total emission from the surface,

$$E_A = \int_A \epsilon\sigma T^4 dA = \int_0^{L_y}\int_0^{L_z} \epsilon\sigma T^4\,\mathrm{d}z\,\mathrm{d}y. \tag{15}$$

As for volume emission the next property of the photon bundle to be determined is the wavenumber. The corresponding CDF of the emission wavenumber is

$$R_\eta = \frac{1}{\epsilon\sigma T^4}\int_0^{\eta} \epsilon_\eta E_{b\eta}\,\mathrm{d}\eta. \tag{16}$$

Once the emission location and wavenumber have been chosen, the directions of emission can be determined from the CDF's of azimuthal and polar angles [1]. For an isotropic and diffuse surface, these are

$$R_\psi = \frac{\psi}{2\pi}, \quad R_\theta = \sin^2\theta. \tag{17}$$

The random number relation for surface absorption is straightforward. When radiative energy impinges on an opaque surface, the fraction α'_η is absorbed while the remainder, $1-\alpha'_\eta$, is reflected, where α'_η is the spectral directional absorptance. For a diffuse reflector, the CDF's of the reflection directions are

$$R_{\psi_r} = \frac{\psi_r}{2\pi}, \quad R_{\theta_r} = \sin^2\theta_r. \tag{18}$$

In the most general case, the directions of reflection depend on the bidirectional reflection function of the material. Their CDF's can be found in [1] (Chapter 20).

Photon bundles incident on a "cold" radiation boundary (e.g., the $-x$ boundary in Fig. 1) simply are removed from the calculation.

4. High-order numerical implementation of the photon Monte Carlo method

The photon Monte Carlo method described in the previous section is applicable to thermal radiation problems of any configuration. The underlying DNS code, however, was developed only for canonical configurations using a Cartesian coordinate system. This section, therefore, will only consider such configurations. Moreover, the mesh system on which the new high-order photon Monte Carlo scheme will be built corresponds to a structured grid with directionally uniform grid spacing, as required by the compact finite-difference schemes in the underlying DNS code [26]. A photon Monte Carlo method is intrinsically a three-dimensional method; i.e., photon bundles need to be traced in three-dimensional computational domains to correctly predict optical thickness and energy absorption along their paths. For physically one- or two-dimensional radiation problems, the statistical error can be reduced by averaging over planes or lines along the redundant directions introduced into the three-dimensional photon Monte Carlo simulations. The underlying DNS code solves the unsteady governing equations. Therefore, for physically stationary problems or problems whose flow fields vary slowly with time, statistical error in numerical solutions can be further reduced by averaging over time.

The remainder of this section describes the high-order numerical implementations of the essential elements of the photon Monte Carlo method introduced in the previous section. Without loss of generality, the three-dimensional computational domain is taken to have dimensions of $[0,L_x]\times[0,L_y]\times[0,L_z]$. The numbers of grid points in the x, y, and z-directions are N_x, N_y, and N_z, and the corresponding grid spacings are denoted by $h_x = L_x/(N_x-1)$, $h_y = L_y/(N_y-1)$, and $h_z = L_z/(N_z-1)$, respectively.

4.1. Emission

Determination of emission locations of photon bundles requires knowledge of the CDF's of emission positions (Eqs. (6) and (7)). For a given flowfield and specified $\kappa_P = \kappa_P(\underline{Y},T,p)$ in a three-dimensional configuration, the discrete values of total emissive power at grid points $(x_i,y_j,z_k)\in[1,N_x]\times[1,N_y]\times[1,N_z]$, $E_{ijk}\equiv(4\kappa_P\sigma T^4)|_{(x_i,y_j,z_k)}$, can be readily calculated; the SI dimensions of E_{ijk} are [W/m^3]. Defining a continuous function $F_1(x,y,z)\equiv 4\kappa_P\sigma T^4$ such that $F_1(x_i,y_j,z_k)=E_{ijk}$, the integral $\int_0^z F_1(x_i,y_j,z)\,\mathrm{d}z$ can be evaluated numerically for any (i,j) index pair (i.e., along a $x=x_i=$ const., $y=y_j=$ const. line) by approximating $F_1(x_i,y_j,z)$ by E_{ijk}'s ($k=1,\ldots,N_z$) using a high-order scheme. Note that $\int_0^z F_1(x_i,y_j,z)\,\mathrm{d}z$ is the cumulative distribution of emission along the line in the three-dimensional configuration. When $z=L_z$, the integration gives the total emissive power from the line ($x=x_i$, $y=y_j$),

$$\int_0^{L_z} F_1(x_i,y_j,z)\,\mathrm{d}z \equiv E_{ij}. \tag{19}$$

Here E_{ij} has units of [W/m^2], and the CDF of the emission z-location on the line ($x=x_i, y=y_j$) is

$$R_{z,ij} = \frac{\int_0^z F_1(x_i,y_j,z)\,\mathrm{d}y}{E_{ij}}. \tag{20}$$

Next, we define $F_2(x,y)\equiv\int_0^{L_z}F_1(x,y,z)\,\mathrm{d}z=\int_0^{L_z}(4\kappa_P\sigma T^4)\,\mathrm{d}z$ with $F_2(x_i,y_j)=E_{ij}$; i.e., the E_{ij}'s are the discrete values of $F_2(x,y)$ at grid points $(x_i,y_j)\in[1,N_x]\times[1,N_y]$ in the x–y plane. Since the E_{ij}'s are available after

the first step, the $F_2(x_i, y)$ can be approximated by the E_{ij}'s ($j = 1, \ldots, N_y$) to any order and, therefore, the cumulative distributions of $F_2(x_i, y)$ ($i \in [1, N_x]$) can be numerically calculated. Specifically, the total emission from line $x = x_i$ in the x–y plane is

$$\int_0^{L_y} F_2(x_i, y)\,\mathrm{d}y = \int_0^{L_y}\int_0^{L_z} F_1(x_i, y, z)\,\mathrm{d}z\,\mathrm{d}y = \int_0^{L_y}\int_0^{L_z} (4\kappa_P\sigma T^4)|_{x=x_i}\,\mathrm{d}z\,\mathrm{d}y \equiv E_i, \tag{21}$$

where E_i has units of [W/m]. Eq. (21) indicates that E_i is actually the total emission from the plane $x = x_i$ in the three-dimensional configuration. With E_i available, the CDF of the emission y-location on line $x = x_i$ in the x–y plane is

$$R_{y,i} = \frac{\int_0^y F_2(x_i, y)\,\mathrm{d}y}{E_i}. \tag{22}$$

Finally, we define $F_3(x) \equiv \int_0^{L_y} F_2(x, y)\,\mathrm{d}y = \int_0^{L_y}\int_0^{L_z}(4\kappa_P\sigma T^4)\,\mathrm{d}z\,\mathrm{d}y$. Then $F_3(x_i) = E_i$; i.e., E_i's are discrete values of $F_3(x)$ at grid points $x = x_i \in [1, N_x]$. Estimating $F_3(x)$ from the E_i ($i = 1, \ldots, N_x$), the cumulative distribution of $F_3(x)$, $\int_0^x F_3(x)\,\mathrm{d}x$, can be determined. In particular, when $x = L_x$, the total emission from the gas volume V is obtained,

$$\int_0^{L_x} F_3(x)\,\mathrm{d}x = \int_0^{L_x}\int_0^{L_y}\int_0^{L_z}(4\kappa_p\sigma T^4)\,\mathrm{d}z\,\mathrm{d}y\,\mathrm{d}x = E_V, \tag{23}$$

and the CDF of the emission x-location on the one-dimensional line is

$$R_x = \frac{\int_0^x F_3(x)\,\mathrm{d}x}{E_V}. \tag{24}$$

Eqs. (19)–(24) all involve one-dimensional integration. To illustrate the numerical implementation, $\int_0^z F_1(x_i, y_j, z)\,\mathrm{d}z$ is evaluated to fourth-order accuracy as an example. Fig. 2 shows an arbitrary segment in the z-direction, which consists of four consecutive grid points A_1, A_2, A_3, and A_4 whose z-coordinates are denoted by z_{n1}, z_{n2}, z_{n3}, and z_{n4}, respectively. Since the values of F_1 at all grid points (i.e., E_{ijk}'s) are known, the spatial distribution of F_1 within $\overline{A_1A_4}$ can be approximated using the one-dimensional Lagrange interpolation formula,

$$\begin{aligned} F_1(z) = {} & \frac{(z-z_{n2})(z-z_{n3})(z-z_{n4})}{(z_{n1}-z_{n2})(z_{n1}-z_{n3})(z_{n1}-z_{n4})}F_1(A_1) + \frac{(z-z_{n1})(z-z_{n3})(z-z_{n4})}{(z_{n2}-z_{n1})(z_{n2}-z_{n3})(z_{n2}-z_{n4})}F_1(A_2) \\ & + \frac{(z-z_{n1})(z-z_{n2})(z-z_{n4})}{(z_{n3}-z_{n1})(z_{n3}-z_{n2})(z_{n3}-z_{n4})}F_1(A_3) + \frac{(z-z_{n2})(z-z_{n3})(z-z_{n1})}{(z_{n4}-z_{n2})(z_{n4}-z_{n3})(z_{n4}-z_{n1})}F_1(A_4), \end{aligned} \tag{25}$$

where z is in the interval $[z_{n1}, z_{n4}]$.

Consider the evaluation of $\int_{z_{n2}}^z F_1(x_i, y_j, z)\,\mathrm{d}z$ with $z_{n2} \leqslant z \leqslant z_{n3}$. Four quadrature points B_m's ($m \in [1, 4]$) (see Fig. 2) are introduced within $\overline{A_2A_3}$. They are uniformly distributed with $z(B_1) = z(A_2)$ and $z(B_4) = z(A_3)$, and the values of F_1 at B_m are obtained From Eq. (25). With the $F_1(B_m)$'s ($m \in [1, 4]$) known, the cumulative distribution of F_1 along $\overline{A_2A_3}$ can be calculated,

$$\int_0^{z'} F_1(x_i, y_j, z)\,\mathrm{d}z = \frac{1}{4}a_4 z'^4 + \frac{1}{3}a_3 z'^3 + \frac{1}{2}a_2 z'^2 + a_1 z'. \tag{26}$$

Here z' is the local coordinate with point A_2 being the origin, and

$$a_1 = F_1(B_1), \tag{27}$$

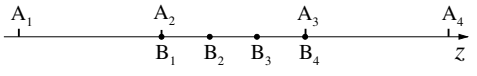

Fig. 2. Interpolation stencil for point A_2 along the z-direction (4th order).

$$a_2 = \frac{1}{2}\frac{2F_1(B_4) - 11F_1(B_1) + 18F_1(B_2) - 9F_1(B_3)}{h_z}, \tag{28}$$

$$a_3 = \frac{-9}{2}\frac{F_1(B_4) - 2F_1(B_1) + 5F_1(B_2) - 4F_1(B_3)}{h_z^2}, \tag{29}$$

$$a_4 = \frac{9}{2}\frac{F_1(B_4) - F_1(B_1) + 3F_1(B_2) - 3F_1(B_3)}{h_z^3}. \tag{30}$$

When $z' = h_z$, Eq. (26) becomes Simpson's 3/8 integration rule and gives the total emission over $\overline{A_2A_3}$,

$$\int_0^{h_z} F_1(x_i, y_j, z)\,\mathrm{d}z = \frac{h_z}{8}[F_1(B_1) + 3F_1(B_2) + 3F_1(B_3) + F_1(B_4)]. \tag{31}$$

Note that the quadrature points are introduced here to neatly express the integral coefficients a_m's ($m \in [1,4]$). The integral $\int_{z_{n2}}^{z} F_1(x_i, y_j, z)\,\mathrm{d}z$ can also be obtained by directly integrating Eq. (25) over $[z_{n2}, z]$. Since the values of F_1 at the four quadrature points are evaluated using Eq. (25), the polynomial formed by them is exactly identical to Eq. (25) and, therefore, both methods give identical answers. The introduction of the quadrature points into the integration process, however, makes Eqs. (26)–(31) formally independent of the choice of the interpolation stencil and the integration segment. These formulae then can be applied to any grid segment in the z-direction without changing their coefficients. In comparison, the values of $F_1(B_m)$ ($m \in [1,4]$) are evaluated using Eq. (25) and thus depend on the definition of the interpolation stencil $\overline{A_1A_2A_3A_4}$. Generally, the stencil is defined in such a way that the target integration segment is as close to the center of the stencil as possible. For any internal grid segment $[z_k, z_{k+1}]$ ($k \in [2, N_z - 2]$), grid points $[z_{k-1}, z_k, z_{k+1}, z_{k+2}]$ are thus chosen to form the four-point interpolation stencil. For the first and last grid segments $[z_1, z_2]$ and $[z_{N_z-1}, z_{N_Z}]$, the stencils are formed by the grid points $[z_1, z_2, z_3, z_4]$ and $[z_{N_z-3}, z_{N_Z-2}, z_{N_z-1}, z_{N_Z}]$, respectively.

With the above preparation, the cumulative distribution of $F_1(x_i, y_j, z)$ along the z-direction can be calculated as follows. For any value $z \in [0, L_z)$, an index n ($1 \leqslant n \leqslant N_Z - 1$) is found such that $z_n \leqslant z < z_{n+1}$, and

$$\int_0^z F_1(x_i, y_j, z)\,\mathrm{d}z = \sum_{k=1}^{n-1}\int_{z_k}^{z_{k+1}} F_1(x_i, y_j, z)\,\mathrm{d}z + \int_{z_n}^{z} F_1(x_i, y_j, z)\,\mathrm{d}z. \tag{32}$$

Therefore, application of Eqs. (26)–(31) to each individual segment with their respective interpolation stencils leads to the value of $\int_0^z F_1(x_i, y_j, z)\,\mathrm{d}z$. When $z = L_z$, Eq. (32) gives E_{ij}: that is, the total emission over the entire z-direction at $(x = x_i, y = y_j)$.

By replacing $F_1(x_i, y_j, z)$ by $F_2(x_i, y)$ and $F_3(x)$, respectively, the above scheme can be used to evaluate $\int_0^y F_2(x_i, y)\,\mathrm{d}y$ ($i \in [1, N_x]$) and $\int_0^x F_3(x)\,\mathrm{d}x$. With the cumulative distributions along all three directions available, the emission position then is determined as follows.

First, for any random number $R_x \in (0,1)$, find the index $l \in [1, N_x - 1]$ such that

$$\frac{\int_0^{x_l} F_3(x)\,\mathrm{d}x}{E_V} \leqslant R_x < \frac{\int_0^{x_{l+1}} F_3(x)\,\mathrm{d}x}{E_V}. \tag{33}$$

Then the corresponding emission x-location is $x = x_l + x'$, where x' is the root of the polynomial,

$$\int_0^{x'} F_3(x)\,\mathrm{d}x = \frac{1}{4}a_4x'^4 + \frac{1}{3}a_3x'^3 + \frac{1}{2}a_2x'^2 + a_1x' = R_x \cdot E_V - \int_0^{x_l} F_3(x)\,\mathrm{d}x. \tag{34}$$

The polynomial coefficients, a_1, a_2, a_3, and a_4, are defined in Eqs. (27)–(30). Eq. (34) can be solved by several methods; here Ridders' method [28] is used to ensure that the root remains in the interval $(0, h_x)$ during iteration.

The second step is to find the emission position in the y-direction at the specified x position for a random number R_y. Assume that the one-dimensional four-point interpolation stencil used to calculate the cumulative distribution of $F_3(x)$ within the segment $[x_l, x_{l+1}]$ corresponds to the grid points $[x_{l-1}, x_l, x_{l+1}, x_{l+2}]$. Then at each stencil point x_i ($i = l-1, l, l+1, l+2$) an emission y-location, y_i, can be determined for the given $R_y \in (0,1)$,

$$y_i = y_{i_m} + y_i', \tag{35}$$

where the index $i_m \in [1, N_y - 1]$ and y_i' are, respectively, determined by

$$\frac{\int_0^{y_{i_m}} F_2(x_i, y)\,\mathrm{d}y}{E_i} \leqslant R_y < \frac{\int_0^{y_{i_m+1}} F_2(x_i, y)\,\mathrm{d}y}{E_i}, \tag{36}$$

$$\int_0^{y_i'} F_2(x_i, y)\,\mathrm{d}y = \frac{1}{4}a_3 y_i'^4 + \frac{1}{3}a_2 y_i'^3 + \frac{1}{2}a_1 y_i'^2 + a_0 y_i' = R_y \cdot E_i - \int_0^{y_{i_m}} F_2(x_i, y)\,\mathrm{d}y. \tag{37}$$

Once the y_i's at each of the four x_i's ($i = l-1, l, l+1, l+2$) have been found, the emission y-location at x is determined by one-dimensional fourth-order interpolation,

$$y(x) = \sum_{l-1 \leqslant i \leqslant l+2} \left[\prod_{\substack{l-1 \leqslant p \leqslant l+2 \\ p \neq i}} \frac{x - x_p}{x_i - x_p} \right] y_i. \tag{38}$$

Finally, the emission z-locations are determined. With y known, the nearest y-grid index $m \in [1, N_y - 1]$ is found such that $y_m \leqslant y < y_{m+1}$. Assume that the four-point interpolation stencil in the y-direction for the segment $[y_m, y_{m+1}]$ corresponds to $[y_{m-1}, y_m, y_{m+1}, y_{m+2}]$. Along with the stencil in the x-direction, a two-dimensional stencil is formed, which consists of 16 grid points (x_i, y_j) $(i = l-1, l, l+1, l+2;\ j = m-1, m, m+1, m+2)$. For a random number $R_z \in (0, 1)$, the emission z-location, z_{ij}, at each point (x_i, y_j) in that two-dimensional stencil is determined by

$$z_{ij} = z_{ij_r} + z_{ij}', \tag{39}$$

where the index $ij_r \in [1, N_z - 1]$ and z_{ij}' are, respectively, determined by

$$\frac{\int_0^{z_{ij_r}} F_3(x_i, y_j, z)\,\mathrm{d}z}{E_{ij}} \leqslant R_z < \frac{\int_0^{z_{ij_r+1}} F_3(x_i, y_j, z)\,\mathrm{d}z}{E_{ij}}, \tag{40}$$

$$\int_0^{z_{ij}'} F_3(x_i, y_j, z)\,\mathrm{d}z = \frac{1}{4}a_3 z_{ij}'^4 + \frac{1}{3}a_2 z_{ij}'^3 + \frac{1}{2}a_1 z_{ij}'^2 + a_0 z_{ij}' = R_z \cdot E_{ij} - \int_0^{z_{ij_r}} F_3(x_i, y_j, z)\,\mathrm{d}z. \tag{41}$$

With all z_{ij}'s ($i = l-1, l, l+1, l+2;\ j = m-1, m, m+1, m+2$) available, the emission z-location at (x, y) is determined by the two-dimensional fourth-order interpolation formula,

$$z(x, y) = \sum_{\substack{l-1 \leqslant i \leqslant l+2 \\ m-1 \leqslant j \leqslant m+2}} \left[\prod_{\substack{l-1 \leqslant p \leqslant l+2 \\ p \neq i}} \frac{x - x_p}{x_i - x_p} \right] \left[\prod_{\substack{m-1 \leqslant q \leqslant m+2 \\ q \neq j}} \frac{y - y_q}{y_j - y_q} \right] z_{ij}. \tag{42}$$

After z is obtained, z's nearest grid index is found; it is denoted here as r with $z_r \leqslant z < z_{r+1}$.

It can be observed that the above procedure involves one- and two-dimensional interpolations and one-dimensional numerical integration. To extend the scheme to any order n ($n \geqslant 2$), one needs only to modify the interpolation stencils employed in the procedure so that they are formed by n and $n \times n$ grid points for one- and two-dimensional interpolations, respectively. The one-dimensional integration scheme also is changed accordingly.

The choice of emission wavenumber depends on the conditions at the emission position (x, y, z). For a given position (x, y, z) and a random number R_η, the emission wavenumber is determined from Eq. (8). For a participating medium containing absorbing/emitting molecular gases, a narrow band model should be applied to treat spectral-line-structure effects [1] (Chapter 20). For gray media, Eq. (8) is not needed.

The emission direction is readily obtained by inverting Eq. (9) for random numbers R_ψ and $R_\theta \in (0, 1)$, without numerical error.

4.2. Tracing and absorption

At the tracing stage an energy partitioning scheme is adopted. Therefore, the energy of each photon bundle is gradually attenuated due to absorption until: (1) the bundle leaves the domain or hits a wall and is absorbed; or (2) its energy is depleted to zero. The path of each photon bundle traveling through the medium is partitioned into multiple segments (or propagation steps). Optical thickness is calculated for each step to determine the fraction of radiant energy deposited into the corresponding layer. Theoretically, the sizes of the propagation steps can be arbitrarily chosen as long as the optical thickness is evaluated with an accuracy that is consistent with that of the emission treatment. However, as will be explained in Section 4.4, determination of the radiation source term at each grid point requires the knowledge of the net radiant energy through the boundaries of an associated control volume. The boundary planes of the control volumes and the grid planes are, therefore, used here to partition the propagation paths of photon bundles, and each resultant segment is considered as a propagation step. Since the boundary planes of the control volumes are centered between the grid planes (see Fig. 3), the largest propagation step would be $S_{\max} = \sqrt{h_x^2 + h_y^2 + h_z^2}/2$, i.e., smaller than $\max(h_x, h_y, h_z)$ and, thus, no further partitioning is needed. Simpson's 3/8th rule then can be used directly to integrate κ_P over the step without loss of accuracy. That is,

$$\int_0^S \kappa_P \, \mathrm{d}s = \frac{S}{8}[\kappa_{P,0} + 3\kappa_{P,1} + 3\kappa_{P,2} + \kappa_{P,3}], \tag{43}$$

where the $\kappa_{P,l}$'s ($l \in [0,3]$) are the absorption coefficients at $\vec{x}_l = \vec{x}_0 + (l/3)S\hat{s}$ with $\vec{x}_0$ being the starting position vector for the current propagation step. Note that κ_P is a function of local temperature, species mass fractions, and pressure, whose values are determined by using Lagrangian fourth-order (in the present example) three-dimensional interpolation. The interpolation formula is given in Appendix B.

4.3. Boundary conditions

When a photon bundle reaches a periodic boundary, it re-enters the computational domain through the opposite boundary. For example, if the planes $y = 0$ and $y = L_y$ are corresponding periodic boundaries and a photon bundle reaches plane $y = 0$ at a coordinate of $(x, 0, z)$, its new location will be (x, L_y, z). Other properties of the photon bundle, such as the propagation direction and the radiant energy it carries, remain unchanged.

At a radiative boundary, surface emission needs to be considered. Generally, for any given distribution of temperature and surface emittance, the emission properties (position, wavelength, and direction) of photon

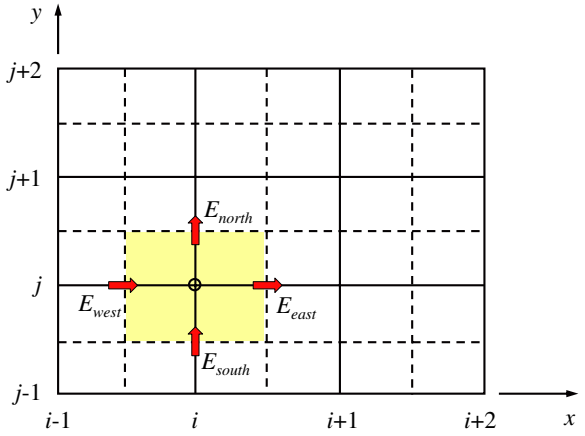

Fig. 3. Interpolation stencil for evaluation of radiation source term (2-D).

bundles leaving a radiative boundary are determined in a similar manner as for emission from within the volume, and the procedures and numerical schemes developed in the previous subsections are applicable.

Two types of radiative surfaces are considered in the present work: "cold" and "hot" boundaries. Both are treated as black surfaces and thus absorb any photon bundles that reach them from inside the volume. At the "cold" boundary, the surface temperature is assigned to be 0 K, and no surface emission occurs at that boundary. At the "hot" boundary, radiative equilibrium is assumed; i.e., the total radiant energy leaving the boundary is equal to that absorbed by the boundary. For a diffuse emitter, this condition is implemented in the following manner. Every time that a photon bundle reaches a "hot" boundary and is absorbed, a new photon bundle is emitted from the boundary into the domain. The emission position and the direction of the new photon bundle are chosen randomly according to their respective uniform distribution functions. Other properties, such as the wavenumber and the radiant energy, are set to those of the photon bundle that was just absorbed.

4.4. Radiation source term

The underlying DNS code solves the differential forms of the conservation equations using a finite-difference method and, therefore, requires the radiation source term at each grid point. To illustrate the high-order numerical scheme for evaluation of the source term, a two-dimensional example is considered. Fig. 3 shows the control volume associated with grid point (x_i, y_j); the control volume is formed by lines $x = x_{i-1/2}$, $x = x_{i+1/2}$, $y = y_{j-1/2}$, and $y = y_{j+1/2}$ and will be referred to hereafter as V_{ij}. The figure also shows the net radiant energy through the four boundaries of the control volume that are denoted as E_{west}, E_{east}, E_{south}, and E_{north}, respectively (units of [W]).

We introduce $\Delta E_x \equiv E_{\text{west}} - E_{\text{east}}$, $\Delta E_y \equiv E_{\text{south}} - E_{\text{north}}$, and $\Delta E_{ij} \equiv \Delta E_x + \Delta E_y$. Then ΔE_{ij} is the total radiant energy deposited in V_{ij}, and is related to the local radiative source through

$$\Delta E_{ij} = \int_{V_{ij}} Q_{\text{rad}} \, \mathrm{d}V, \tag{44}$$

where $Q_{\text{rad}} \equiv -\nabla \cdot \vec{q}_{\text{rad}}$.

Due to the carefully designed tracing scheme described in Section 4.2, E_{west}, E_{east}, E_{south}, and E_{north} are available immediately after the tracing of all photon bundles is done; ΔE_{ij} is thus a known quantity. To find Q_{rad} at grid point (x_i, y_j), a two-dimensional interpolation stencil is defined for V_{ij}, formed by $[x_{i-1}, x_i, x_{i+1}, x_{i+2}] \times [y_{j-1}, y_j, y_{j+1}, y_{j+2}]$ in Fig. 3. The spatial distribution of Q_{rad} is approximated in V_{ij} by the Q_{rad} at the stencil points using the two-dimensional Lagrangian interpolation formula,

$$Q_{\text{rad}}(x,y) = \sum_{\substack{i-1 \leqslant l \leqslant i+2 \\ j-1 \leqslant m \leqslant j+2}} \left[\prod_{\substack{i-1 \leqslant p \leqslant i+2 \\ p \neq l}} \frac{x - x_p}{x_l - x_p} \right] \left[\prod_{\substack{j-1 \leqslant q \leqslant j+2 \\ q \neq m}} \frac{y - y_q}{y_m - y_q} \right] Q_{\text{rad},lm}. \tag{45}$$

Substitution of Eq. (45) into Eq. (44) leads to an equation that is a linear function of the $Q_{\text{rad},lm}$ ($l = i-1, i, i+1, i+2$; $m = j-1, j, j+1, j+2$). This procedure is applied to all grid points, resulting in a sparse linear system for the $Q_{\text{rad},ij} \in [1, N_x] \times [1, N_y]$ that can be solved using any linear solver. The coefficient matrix of the resultant linear system depends only on the coordinates of the grid points. For a given radiation problem and a prespecified order of accuracy, this matrix only needs to be calculated once. The three-dimensional counterpart of Eq. (45) for any order of accuracy takes the form of Eq. (B.1) with the replacement of function $F(x,y,z)$ by $Q_{\text{rad}}(x,y,z)$.

4.5. Comments on choice of interpolation functions

Here high-order Lagrange polynomials have been adopted to interpolate function values inside the computational domain. Compared to alternative interpolation methods, such as splines, Lagrange polynomials have two attractive features: their formulations are simple and intuitive, and their three-dimensional formulations can be readily derived from one-dimensional formulations of the same order. The potential interpolation

oscillations associated with high-order Lagrange polynomials are well controlled here because: (i) the grid systems adopted in DNS are directionally uniform and dense; and (ii) inside the computational domain, interpolation is done only for the points in the center regions of the interpolation stencils.

5. Numerical tests

In this section, the high-order photon Monte Carlo scheme developed in Section 4 is tested for several radiation problems. Nondimensional forms of the governing equations are solved, as discussed earlier. The dimensionless quantities and variables are denoted by a superscript '+.' Appendix A shows the nondimensionalization of the radiation source term in the energy equation. The dimensionless forms of the other equations are given in Ref. [25]. A detailed assessment of numerical errors is provided in Section 5.1. Sections 5.2 and 5.3 provide examples of applications of the new algorithm to laminar and turbulent premixed flames, respectively.

5.1. One-dimensional radiation with specified temperature field

Here the accuracy of the high-order photon Monte Carlo scheme is established using a one-dimensional radiation problem. The configuration is a stationary, nonscattering gray medium enclosed by two cold, black bounding surfaces separated by a distance $L^+ = 0.6$. The temperature field is specified as

$$T^+(x^+) = 5\left[\sin\left(4\pi\left(\frac{x^+}{L^+} - \frac{1}{8}\right)\right) + 2\right]. \tag{46}$$

The Planck-mean absorption coefficient of the medium is a function of local temperature:

$$\kappa_p^+(T^+) = c_0 + c_1\left(\frac{8}{T^+}\right) + c_2\left(\frac{8}{T^+}\right)^2 + c_3\left(\frac{8}{T^+}\right)^3 + c_4\left(\frac{8}{T^+}\right)^4 + c_5\left(\frac{8}{T^+}\right)^5, \tag{47}$$

where the coefficients are $c_0 = -0.23093$, $c_1 = -1.12390$, $c_2 = 9.41530$, $c_3 = -2.99880$, $c_4 = 0.51382$, $c_5 = -1.86840 \times 10^{-5}$, respectively; these are taken from a radiation model suggested for water vapor [29]. Fig. 4 shows the spatial distribution of the temperature and the Planck-mean absorption coefficient for this problem, while Fig. 5 shows the profiles of the corresponding theoretical solutions for the radiative heat flux and the source term (see Appendix C: Eqs. (C.1)–(C.3)).

A series of numerical simulations for this one-dimensional radiation problem was conducted using a three-dimensional configuration to test the high-order photon Monte Carlo method that has been developed here. The computational domain is a cubic box of size $(L^+)^3 = 0.6^3$ with the east and west sides being the bounding surfaces. Periodic boundary conditions are enforced on the other four sides to simulate an infinite one-dimensional slab. The grid systems adopted in all calculations were uniform in all three directions.

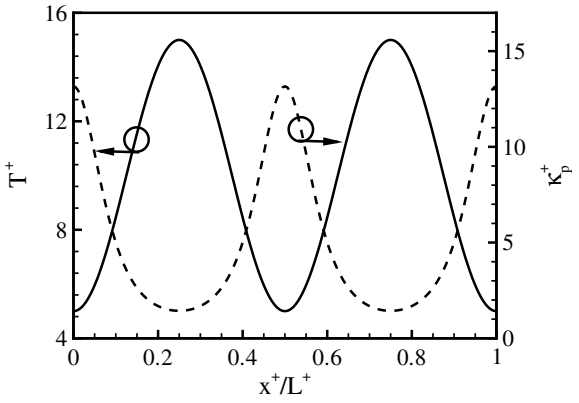

Fig. 4. Distributions of temperature and Planck-mean absorption coefficient in the one-dimensional radiation problem.

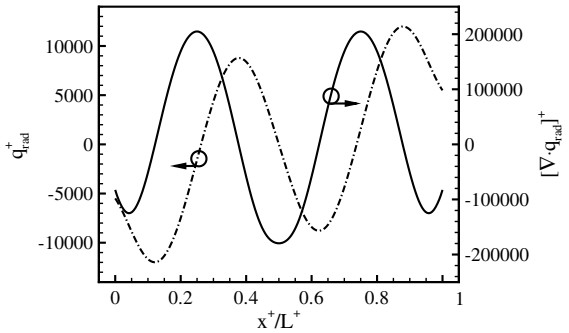

Fig. 5. Spatial distributions of theoretical solutions of radiative heat flux and radiation source term in the one-dimensional radiation problem.

5.1.1. Systematic error

First, the systematic error of the photon Monte Carlo scheme is quantified. The grid system for this study was $7 \times 7 \times 7$. This can be thought of as a small subdomain of a mesh that would be used for full-scale simulation. Because of the interpolation schemes employed in the photon Monte Carlo code, the effective temperature profile that is simulated is different from the sinusoidal profile shown in Fig. 4 and depends on the interpolation order. Fig. 6 shows the implied spatial distributions of temperature for several orders of interpolation scheme, while Fig. 7 shows the corresponding theoretical radiative heat fluxes; there the subscript

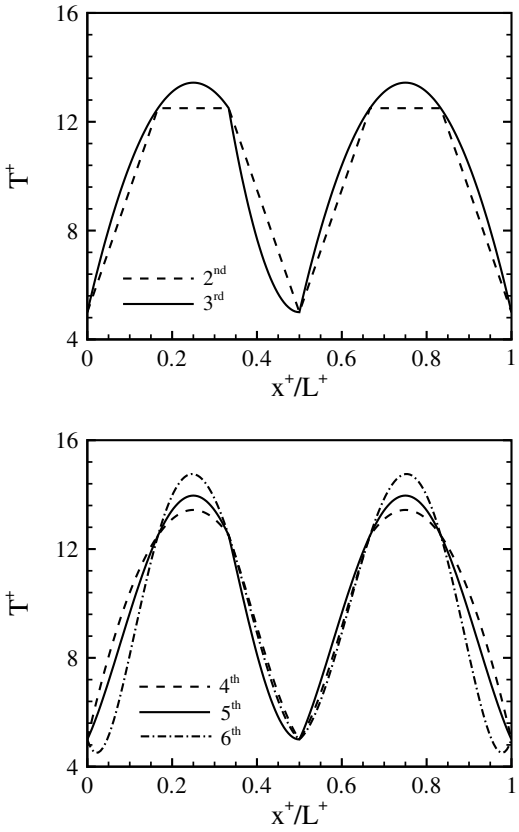

Fig. 6. Implied temperature profiles in photon Monte Carlo simulations for various interpolation orders in the one-dimensional radiation problem.

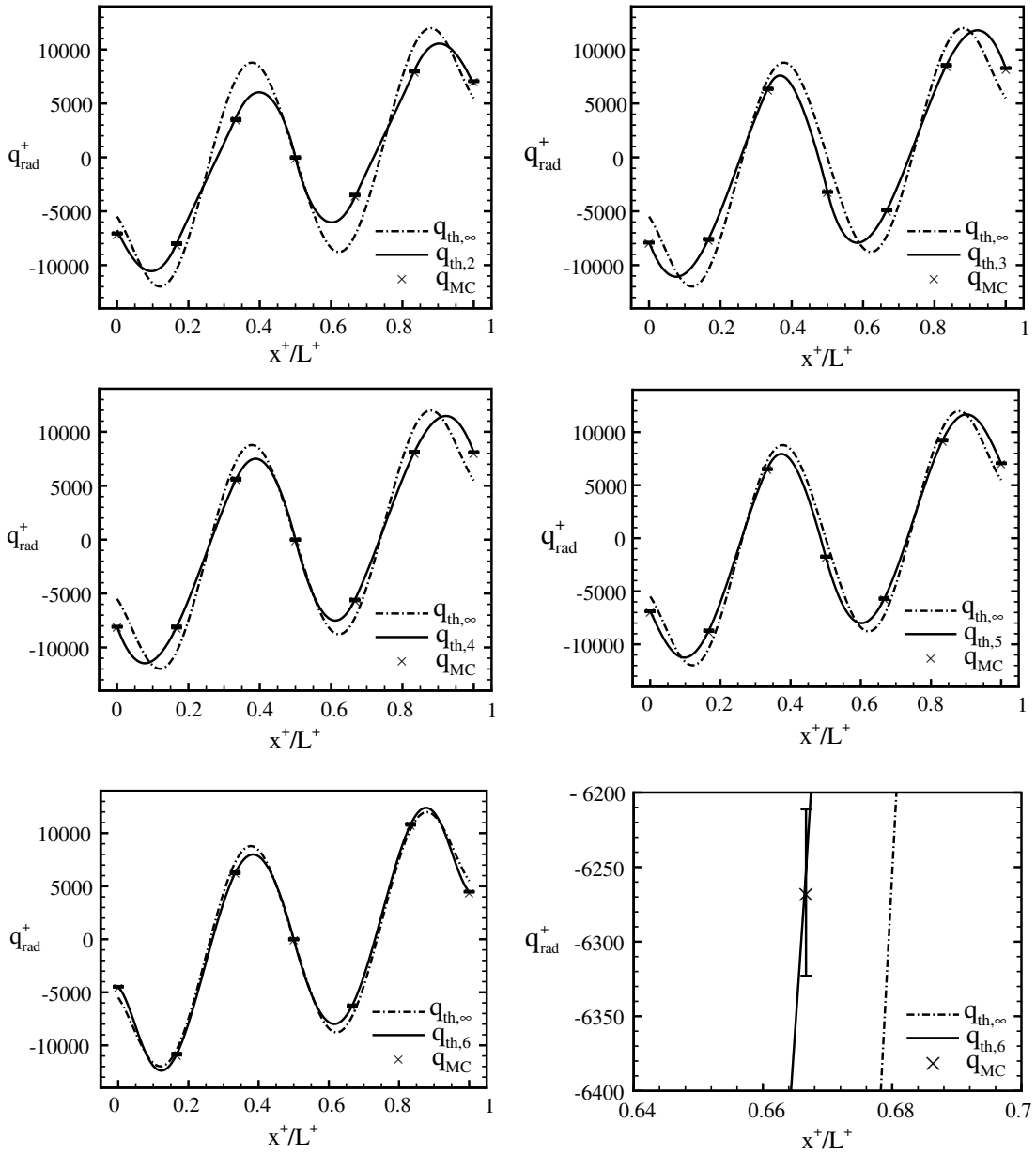

Fig. 7. Theoretical and numerical solutions of radiative heat flux for various orders of accuracy in the one-dimensional radiation problem. The lower-right hand frame is a "zoom-in" on a small region of the 6th order plot to show the statistical error (error bars) more clearly.

"th, ∞" indicates the theoretical solution corresponding to the sinusoidal temperature profile, and the subscript "th, n" for an integer n indicates the theoretical solution obtained with a temperature profile constructed using the nth-order interpolation scheme from Fig. 6. Also shown in Fig. 7 are the statistical averages and standard deviations of the y–z plane-averaged numerical results from the photon Monte Carlo simulations; these are designated by a subscript "MC." Ten trials were carried out for each case with each trial involving an average of 1000 photon bundles per computational cell. Here the standard deviations are much smaller than the magnitudes of the radiative heat flux at grid points, and the lower and upper limits of the error bars appear merged in Fig. 7; a "zoom-in" for one case (6th order) is included to show the magnitude of the statistical error. It can be observed that the numerical predictions agree very well with their respective theoretical

solutions based on the implied temperature profiles for all orders of accuracy. As the order of spatial accuracy increases, the numerical solution approaches the theoretical solution for the sinusoidal temperature profile.

5.1.2. Statistical error

Next, the statistical error is examined for the same $7 \times 7 \times 7$ grid system. The average number of photon bundles per computational cell, N_{pc}, was increased systematically from 100 to 1000, 10,000, and 100,000. For each value of N_{pc} and each order of accuracy, 10 independent trials were conducted. The standard deviations of the y–z plane-averaged radiative heat fluxes at $x^+/L^+ = 0$, 1/6, 1/3 and 1/2 were calculated for each case, and their variations with N_{pc} are plotted in Fig. 8. There σ_{10} denotes standard deviation normalized by

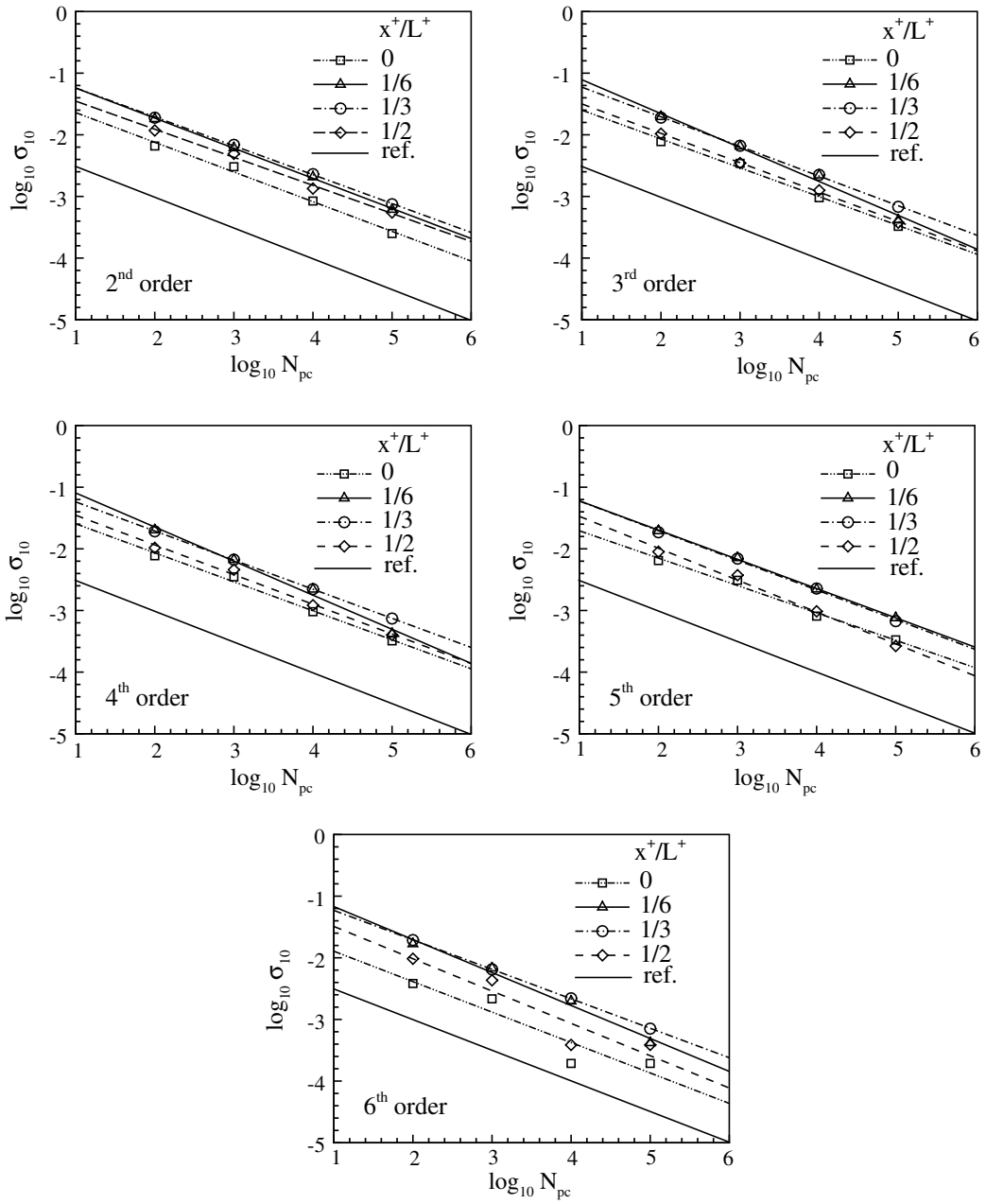

Fig. 8. Statistical errors in radiative heat flux for various orders of accuracy in the one-dimensional radiation problem.

$q^+ - \max$, the maximum value of the radiative heat flux from the theoretical temperature distribution. The solid line with the legend "ref." in each frame is a reference line that has a slope of $-1/2$, corresponding to the expected behavior of the standard deviation in a Monte Carlo method [23,24,30],

$$\sigma_{10} \sim N_{\mathrm{pc}}^{-1/2}. \tag{48}$$

5.1.3. Spatial discretization error

Third, the discretization error is examined. For each order of accuracy, the problem was solved first on the $7 \times 7 \times 7$ grid. Then the number of computational cells in the x-direction, N_{cells}, was sequentially doubled from 6 to 12, 24, 48, 96, etc., with the numbers of grid points in the y- and z-directions fixed at 7. Again, this can be interpreted as a subdomain of a mesh from a larger simulation corresponding to two wavelengths of variation in the temperature profile. For each grid system, 10 trials were conducted to obtain statistical averages and standard deviations of the y–z plane-averaged radiative heat flux along the x-direction, and (with one exception) the number of photon bundles per cell was determined such that the statistical error remains smaller than the discretization error $|q^+_{\mathrm{MC}} - q^+_{\mathrm{th},\infty}|$ at each grid point. Fig. 9 shows the variation of discretization error $\epsilon_{\mathrm{MC},\infty}$ with the number of computational cells in the x-direction at several x-locations, where $\epsilon_{\mathrm{MC},\infty} \equiv |q^+_{\mathrm{MC}} - q^+_{\mathrm{th},\infty}|/q^+_{\mathrm{max}}$. Also shown in Fig. 9 are reference lines having slopes of $-n$, where n is the order of accuracy of the scheme tested. In all cases and at most x-locations shown in the figure, the curves obtained from the numerical simulations are parallel to or steeper than their respective reference lines, confirming that the scheme does achieve the claimed order of spatial accuracy. An exception occurs at $x^+/L^+ = 1/2$ with the second-order scheme. At that location, the radiative heat flux is close to zero (Fig. 5), and the local error is several

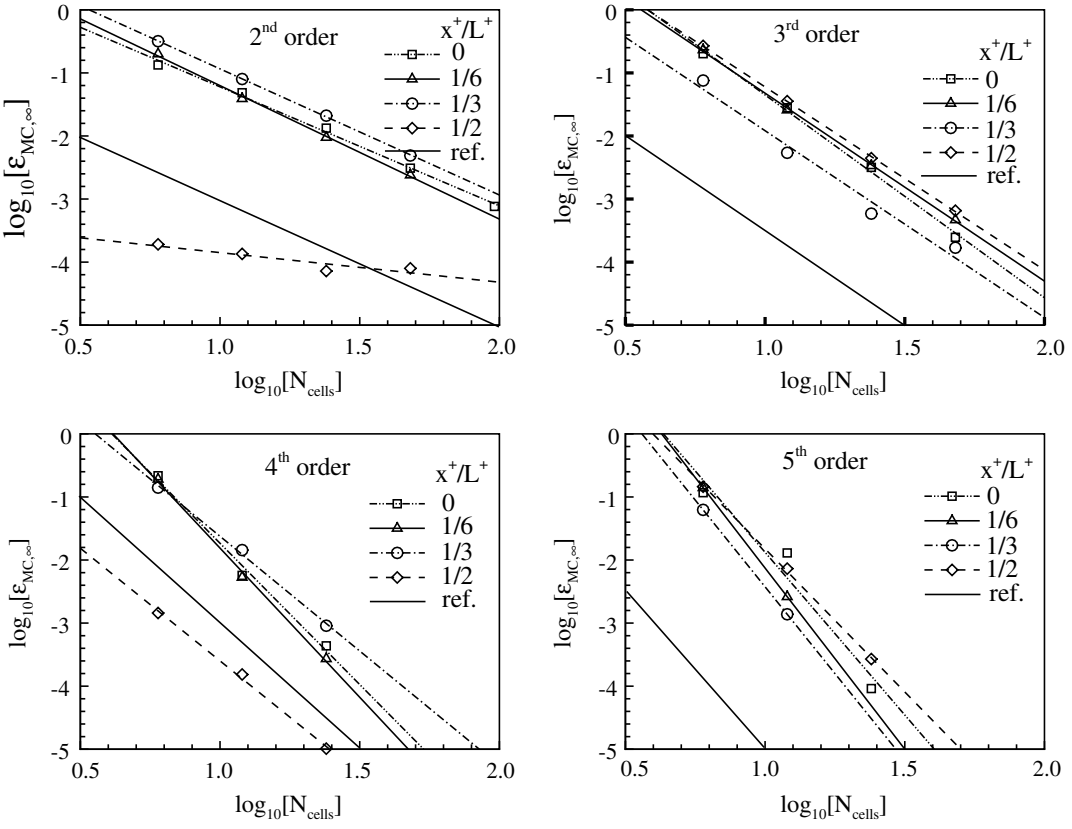

Fig. 9. Variation of discretization error of radiative heat flux with number of computational cells in the one-dimensional radiation problem.

orders of magnitude lower than at the other locations plotted. The absence of a $-1/2$ slope locally is not a concern.

Fig. 10 shows an estimate of the minimum number of photon bundles per cell, $N_{pc,min}$, that is required to keep the statistical error smaller than the spatial discretization error. This value represents an average over the spatial locations plotted in Figs. 8 and 9, and uses the $N_{pc}^{-1/2}$ scaling for statistical error that has been confirmed in Fig. 8. The abscissa of Fig. 10 (N_{cells}) is the number of cells per wavelength in the temperature profile (Fig. 5). Fig. 10 shows that for a given spatial order, the minimum number of photon bundles required to keep the statistical error below the discretization error increases with increasing spatial resolution. For a fixed spatial resolution N_{cells}, $N_{pc,min}$ increases with the order of accuracy. The solid horizontal line through zero corresponds to 1000 photon bundles per cell; this represents an approximate practical upper limit on what would be practicable for DNS of a turbulent flame. For dense grids and without introduction of any additional variance reduction strategies, second- and third-order schemes can be used effectively.

5.1.4. Radiation source term

Finally, the accuracy of the radiation source term from the photon Monte Carlo simulation is examined. The analysis strategy is the same as for the examination of the discretization error of the radiative heat flux. The variation of the discretization error of the radiation source term versus the number of computational cells at several x-locations is shown in Fig. 11; here $\epsilon_{MC,\infty}$ is defined as $|Q^+_{MC} - Q^+_{th,\infty}|/Q^+_{max}$. Comparison of the

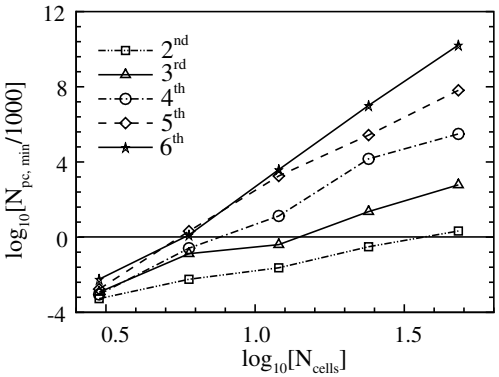

Fig. 10. Variation of minimum number of photon bundles per cell with number of computational cells per wave length.

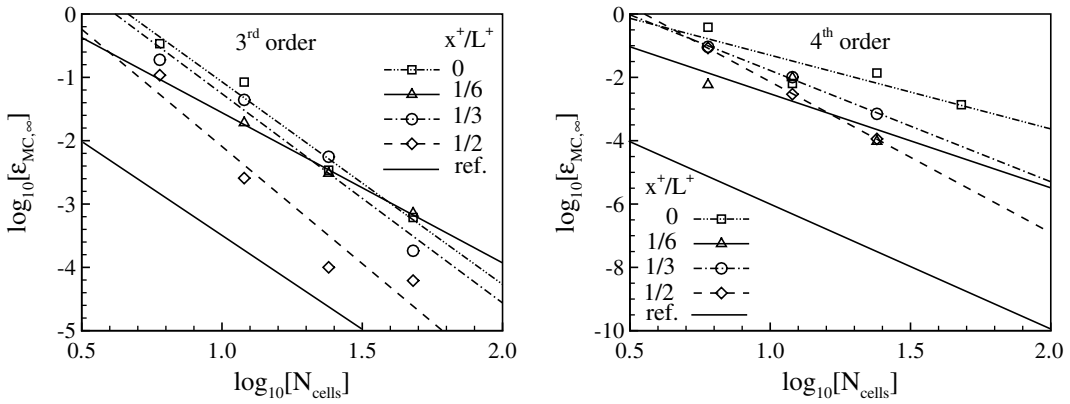

Fig. 11. Variation of discretization error of radiation source term with number of computational cells in the one-dimensional radiation problem.

slopes of the lines obtained via simulation to the reference lines reveals that the numerical predictions of source terms also achieve the expected order of accuracy.

5.2. One-dimensional premixed laminar flame

Tests in the previous subsection have isolated the statistical and discretization errors and confirmed the spatial order of accuracy of the photon Monte Carlo scheme. The method next is applied to a one-dimensional premixed laminar flame. The nondimensional parameters adopted for this case are:

$$Pr = 0.75, \quad Le = 1.0, \quad \alpha = 0.75, \quad \beta = 8.0, \quad Da = 129.616,$$

where Pr and Le are Prandtl number and Lewis number, respectively, and α and β are the reaction parameters introduced in Eq. (1). Da denotes Damköhler number and is defined as $Da = D/S_{L0}^2\Lambda$. Here D and S_{L0} are the species diffusivity and unstretched, adiabatic, laminar flame speed, respectively. The nondimensional coefficient σ^+ in Eq. (A.4) is 10^{-6}, and the Planck-mean absorption coefficient of the fictitious medium is assumed to be a function of the reactant mass fraction as well as temperature to mimic that of water vapor,

$$\overline{\kappa_p}^+(T^+, \widetilde{Y}) = \kappa_p^+(T^+) \cdot (1 - \widetilde{Y}), \tag{49}$$

where $\kappa_p^+(T^+)$ is defined in Eq. (47). With these choices, the ratio of the maximum values of radiation source term to chemical source term in the energy equation is 24%, and the total radiant fraction (ratio of radiation source term to chemical source term integrated over the computational domain) is 11.8%.

The numerical simulation is conducted in a two-dimensional configuration with $L_x^+ = 4.5$ and $L_y^+ = 0.09$. The grid system consists of 451×10 points that are uniformly distributed in the x- and y-directions, respectively. The reactants flow into the domain through the west side and the burnt gases flow out of domain through the east side. The "cold" and "hot" radiation boundary conditions are enforced at the west and east sides, respectively. At the south and north sides, periodic boundary conditions are adopted for both flow and radiation to simulate an infinite slab in the y-direction.

To elucidate the effects of radiation, the calculation was performed in three stages. First, a stationary adiabatic laminar flame solution was established; the flame was stationary for an inflow speed of $S_{L0}^+ = 0.0016$. Next, a new stationary laminar flame solution was established starting with the stationary adiabatic solution as an initial condition, and time marching to a new stationary solution with the radiation source term obtained by solving the RTE using an approximate method (a P1 spherical harmonics method [1]). This accelerates convergence to the steady state; the same steady-state solution is obtained without using P1 as an intermediate. With radiation enabled, the reactants are effectively preheated, resulting a higher flame speed but lower product temperature. A stationary solution was obtained for an inlet velocity of $S_L^+ = 0.0024$, a 50% increase over the adiabatic value. Finally, the photon Monte Carlo method was enabled. Third-order spatial accuracy was used with 500,000 photon bundles per computational time step (123 bundles per cell on average). Statistical error was further reduced by averaging the radiation source term over 100 time steps. The system was again

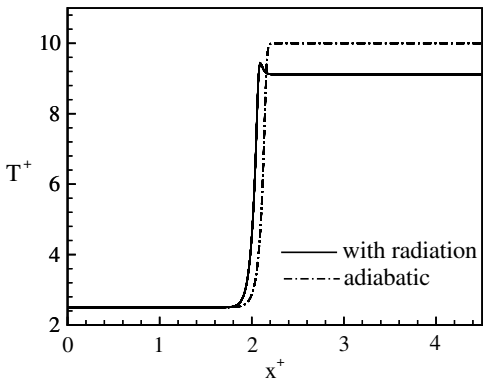

Fig. 12. Spatial distributions of temperature for steady one-dimensional laminar premixed flames with and without radiation.

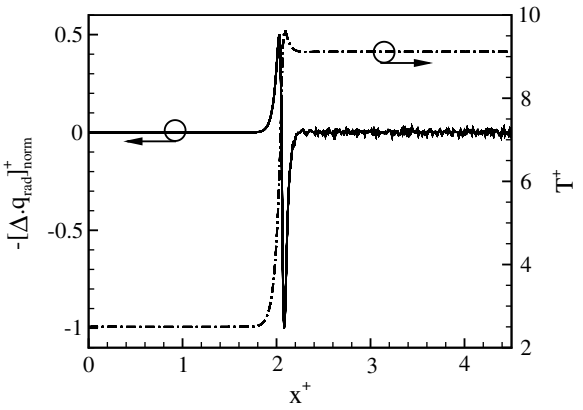

Fig. 13. Spatial distributions of normalized radiation source term and temperature for a steady one-dimensional laminar premixed flame with radiation.

run to steady state. For this simple configuration and radiation properties, only small adjustments were found compared to the converged P1 solution.

Converged steady-state temperature and radiation source term profiles are shown in Figs. 12 and 13. The attenuation of the burned-gas temperature with respect to the adiabatic flame is 9% (Fig. 12) and the shape of the temperature profile with radiation (the peak on the hot side of the reaction zone) is a consequence of the prescribed functional form of $\overline{\kappa_p}^+(T^+, \widetilde{Y})$. Statistical fluctuations in the radiation source term can be seen on the hot product side in Fig. 13. There the radiation source term has been normalized by its maximum value. While these can be reduced by increasing the number of photon bundles and/or by time-averaging for this stationary flame, such measures have not been found to be necessary. For both laminar flames and turbulent flames (Section 5.3), no adverse effects or growing instabilities have been observed.

5.3. Statistically one-dimensional premixed turbulent flame

5.3.1. Example

The final configuration examined is a statistically one-dimensional, turbulent, premixed flame (Fig. 1). Initial results for this configuration have been reported in [31]. Those simulations corresponded to a global radiant fraction of approximately 0.26%, that is, to a case where radiation has little influence on the turbulent flame structure. Here, a two-dimensional simulation with a global radiant fraction of 5.3% is presented. The thermo-chemical and radiation properties adopted are the same as in Section 5.2. This simulation is intended only to demonstrate that the new algorithms can be applied to DNS of turbulent reacting flows. Detailed analysis of the physical effects of thermal radiation and TRI in turbulent reacting flows is beyond the scope of this numerical method paper. Applications of the present algorithms to turbulent premixed and nonpremixed systems can be found in [31–33].

Here the computational domain is a square box of dimension $L^+ = 4.5$, with 451×451 grid points. A third-order photon Monte Carlo method has been used with 10^7 photon bundles traced per computational time step. The initial condition corresponds to the converged stationary one-dimensional laminar solution of Section 5.2. That solution was mapped to the two-dimensional box, and a field of two-dimensional homogeneous isotropic turbulence (turbulence Reynolds number is 64.87; ratio of rms turbulence intensity to laminar flame speed is 20.83) was superposed [31]. The system then was allowed to evolve in time. "Cold" and "hot" radiation boundary conditions were enforced at the west and east faces, respectively, and periodic boundary conditions at the south and north faces.

Instantaneous temperature profiles after the system has evolved for four turbulence eddy turnover times are shown in Fig. 14. The corresponding adiabatic computation also is shown. It can be seen that the product temperature in the flow with radiation is significantly lower than its adiabatic counterpart, and that the local reaction zone structure is modified significantly by radiation.

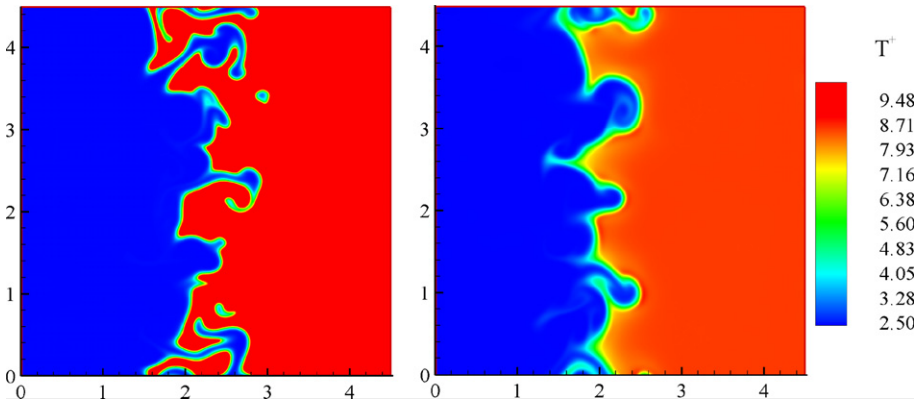

Fig. 14. Instantaneous temperature contours for statistically one-dimensional turbulent premixed flames after four turbulence eddy turn-over times. Left: without radiation; right: with radiation.

5.3.2. Computational issues for turbulent reacting flows

Computational overhead for the photon Monte Carlo method can be substantial. While stable solutions can be obtained using relatively small number of photon bundles, reducing statistical error to levels that are formally below the spatial discretization error requires large numbers of samples and other variance reduction strategies. A few general comments on computational issues for turbulent reacting flows are offered here; further analysis and approaches to reduce the computational overhead are the subjects of ongoing research.

First, the computational effort increases in proportion to the number of photon bundles and the average distance that a bundle travels before being absorbed. For the cases reported in [31], radiation required approximately 10 times the CPU time of the underlying simple-chemistry DNS code. While this is significant, it is important to keep in mind that compared to alternative methods, the photon Monte Carlo method provides an "exact" solution to the RTE that is compatible with the philosophy of DNS, as pointed out in Introduction. Moreover, the implementation is quite general. Nongray radiation properties, scattering, and solid particle (soot) radiation can be included with little additional computational overhead. For computations involving more detailed chemistry (e.g., [34]), the radiation calculation would require little additional computational effort, while the CPU time for the underlying hydro-chemical DNS would increase dramatically; chemical kinetics then would dominate the CPU requirements.

Second, computational efficiency can be enhanced by carefully choosing the number of photon bundles based on the characteristic optical thickness. For a flowfield with low optical thickness, photon bundles can travel a long distance before being absorbed and cross many computational cells. By contrast, in a flowfield with high optical thickness, photon bundles' propagation distances are short. In extreme cases, photon bundles may not even cross one computational cell. Consequently, fewer photon bundles can be used for cases with lower optical thickness to achieve the same statistical accuracy as for cases with higher optical thickness.

Third, the statistical error of the photon Monte Carlo method can be reduced by methods other than increasing the number of photon bundles. For the one-dimensional laminar premixed flame in Section 5.2, for example, averages over time and space can be employed to obtain the distributions of properties along the flame propagation direction. In the statistically one-dimensional turbulent premixed flame of Fig. 14, the computational time step is dictated by a speed-of-sound-based CFL number, and 100 computational time steps correspond to less than 3% of one turbulence eddy turn-over time. Thus, even in turbulent cases, it is possible to employ some time averaging of the radiation source term.

Fourth, the photon Monte Carlo method can be parallelized to take advantage of distributed-memory computers. A spatial domain decomposition is employed in the underlying DNS code. The number of photon bundles emitted from any computational cell is proportional to the local $\kappa_p * T^4$ product. Therefore, the majority of the photon bundles are emitted from the hot product region while only a few are emitted from the cold reactant side. For the statistically one-dimensional premixed turbulent system considered here, then, good load balancing is achieved by decomposing the domain into equally spaced slabs in the y-direction. In each subdomain, a prespecified number of photon bundles is assigned. Their propagation is traced, and those

reaching the subdomain's boundaries are collected until all bundles have reached a subdomain boundary or have been absorbed. Then all bundles are passed to the respective neighboring subdomains. The large message sizes enhance scalability. Nearly linearly scaling has been achieved to date on up to 32 processors.

6. Conclusions

A high-fidelity photon Monte Carlo method has been developed. Its statistical and discretization errors have been isolated and quantified. Formal spatial accuracy of up to sixth order for the radiative heat flux and up to fourth order for the radiation source term has been verified, demonstrating the compatibility of the method with the high-order numerical schemes used in DNS of steady and unsteady, laminar and fully turbulent chemically reacting flows. Computational considerations may limit the number of photon bundles that can be used in practice, and hence limit the spatial discretization accuracy to second or third order, in DNS of turbulent reacting flows. This is expected to be sufficient in most cases. The capability of the photon Monte Carlo method to address radiation heat transfer in chemically reacting flows has been demonstrated through simulations of a one-dimensional laminar premixed flame and a statistically one-dimensional, turbulent premixed flame. Applications of the algorithm to generate new physical insight into thermal radiation and turbulence–radiation interaction in canonical premixed and nonpremixed turbulent, chemically reacting flows have been reported in [31–33]. Further improvements in computational efficiency and variance reduction strategies are the subjects of ongoing research.

Acknowledgements

This work has been supported by the National Science Foundation under Grant Number CTS-0121573 and by the Air Force under Grant Number F49620-99-1-0290. The authors also wish to thank Dr. B. Cuenot at CERFACS for assistance with DNS code.

Appendix A. Nondimensionalization of radiation source term in energy equation

The following reference values have been introduced to nondimensionalize the governing equations, as provided by the underlying DNS code [25]

$$a_{ref}, L_{ref}, t_{ref} = \frac{L_{ref}}{a_{ref}}, T_{ref}, \rho_{ref}, p_{ref}, \mu_{ref}, \nu_{ref}, \lambda_{ref}, c_{p_{ref}},$$

where a is the speed of sound. The above values are defined with respect to a state at "infinity," which can be any state. The sole condition imposed to variables at "infinity" is that the perfect gas relation is satisfied. With these restrictions the reference values can be defined by the "infinity" state as

$$\begin{aligned} &a_{ref} = a_\infty, \quad T_{ref} = (\gamma - 1) \cdot T_\infty, \quad \rho_{ref} = \rho_\infty, \\ &p_{ref} = \rho_\infty \cdot a_\infty^2 = \gamma \cdot p_\infty, \\ &\mu_{ref} = \mu_\infty, \quad \nu_{ref} = \nu_\infty, \quad \lambda_{ref} = \lambda_\infty, \quad c_{p_{ref}} = c_{p_\infty}. \end{aligned}$$

Now consider the energy equation Eq. (2). Its dimensionless form is obtained by dividing it by $[\rho_{ref} a_{ref}^3 / L_{ref}]$. Accordingly, the radiation source term in Eq. (2) becomes

$$\frac{L_{ref}}{\rho_{ref} a_{ref}^3} \cdot [\nabla \cdot \vec{q}_{\mathrm{rad}}] = \frac{L_{ref}}{\rho_{ref} a_{ref}^3} \cdot [\kappa_{P_{ref}} \sigma T_{ref}^4] \cdot [\nabla \cdot \vec{q}_{\mathrm{rad}}]^+ \tag{A.1}$$

where

$$\begin{aligned} [\nabla \cdot \vec{q}_{\mathrm{rad}}]^+ &\equiv \frac{1}{\kappa_{P_{ref}} \sigma T_{ref}^4} [\nabla \cdot \vec{q}_{\mathrm{rad}}] \\ &= 4\kappa_P^+ T^{+4} - \int_0^\infty \kappa_\eta^+ G_\eta^+ \, \mathrm{d}\eta. \end{aligned} \tag{A.2}$$

Here $\kappa_{P_{ref}}$ is the reference value of κ_P and defined by the "infinity" state as $\kappa_{P_{ref}} = \kappa_{P,\infty}$. Other quantities in the above equation are defined as

$$\kappa_P^+ \equiv \frac{\kappa_P}{\kappa_{P_{ref}}}, \quad \kappa_\eta^+ \equiv \frac{\kappa_\eta}{\kappa_{P_{ref}}}, \quad T^+ \equiv \frac{T}{T_{ref}},$$
$$G_\eta^+ \equiv \frac{G_\eta}{\sigma T_{ref}^4}, \quad x^+ \equiv \frac{x}{L_{ref}}, \quad L^+ \equiv \frac{L}{L_{ref}}.$$

Also

$$Re_{ref} \equiv \frac{a_{ref} \cdot L_{ref}}{\nu_{ref}}, \quad Pr_{ref} \equiv \frac{c_{p_{ref}} \cdot \mu_{ref}}{\lambda_{ref}},$$
$$N_{ref} \equiv \frac{\lambda_{ref} \cdot \kappa_{P_{ref}}}{4\sigma \cdot T_{ref}^3}, \quad \tau_{ref} \equiv L_{ref} \cdot \kappa_{P_{ref}},$$

so that

$$\begin{aligned}\frac{L_{ref}}{\rho_{ref} a_{ref}^3} \cdot [\kappa_{P_{ref}} \sigma T_{ref}^4] &= \frac{\lambda_{ref}}{\rho_{ref} \cdot a_{ref} \cdot L_{ref}} \cdot [L_{ref} \cdot \kappa_{P_{ref}}]^2 \cdot \frac{T_{ref}}{a_{ref}^2} \cdot \frac{\sigma T_{ref}^3}{\lambda_{ref} \cdot \kappa_{P_{ref}}} \\ &= \frac{c_{p_{ref}}}{Re_{ref} \cdot Pr_{ref}} \cdot \frac{(\gamma - 1) T_\infty}{a_\infty^2} \cdot \frac{\tau_{ref}^2}{4 N_{ref}} \\ &= \frac{1}{Re_{ref} \cdot Pr_{ref}} \cdot \frac{\tau_{ref}^2}{4 N_{ref}} \equiv \sigma^+. \end{aligned} \tag{A.3}$$

Substitution of Eq. (A.3) into Eq. (A.1) leads to

$$\frac{L_{ref}}{\rho_{ref} a_{ref}^3} \cdot [\nabla \cdot \vec{q}_{\text{rad}}] = \sigma^+ \cdot [\nabla \cdot \vec{q}_{\text{rad}}]^+, \tag{A.4}$$

which is the radiation source term in the dimensionless energy equation.

Appendix B. Three-dimensional interpolation of state quantities at arbitrary locations

In a photon Monte Carlo method, optical thickness needs to be evaluated during the tracing of photon bundles, which requires the knowledge of the absorption coefficient κ along the traveling paths. Generally, κ is a function of temperature, species mass fractions, and pressure whose values are only available at discrete nodal points. Interpolation, therefore, has to be employed to determine those state quantities at any position before calculating κ.

Assume that the interpolation location is (x, y, z) with $x = x_l + \Delta x$, $y = y_m + \Delta y$, and $z = z_r + \Delta z$, where

$$1 \leqslant l < N_x, \quad 0 \leqslant \Delta x < h_x,$$
$$1 \leqslant m < N_y, \quad 0 \leqslant \Delta y < h_y,$$
$$1 \leqslant r < N_z, \quad 0 \leqslant \Delta z < h_z.$$

Also assume that the interpolation stencil is formed by $[x_{i_1}, x_{i_1+1}, \ldots, x_{i_2}] \times [y_{j_1}, y_{j_1+1}, \ldots, y_{j_2}] \times [z_{k_1}, z_{k_1+1}, \ldots, z_{k_2}]$, where

$$i_1 \leqslant l \leqslant i_2, \quad i_2 - i_1 + 1 = n,$$
$$j_1 \leqslant m \leqslant j_2, \quad j_2 - j_1 + 1 = n,$$
$$k_1 \leqslant r \leqslant k_2, \quad k_2 - k_1 + 1 = n.$$

Here n ($\geqslant 2$) is the interpolation order required. Then $F(x, y, z)$ can be calculated from the equation

$$F(x,y,z) = \sum_{\substack{i_1 \leqslant i \leqslant i_2, j_1 \leqslant j \leqslant j_2 \\ k_1 \leqslant k \leqslant k_2}} \left[\prod_{\substack{i_1 \leqslant p \leqslant i_2 \\ p \neq i}} \frac{x - x_p}{x_i - x_p} \prod_{\substack{j_1 \leqslant q \leqslant j_2 \\ q \neq j}} \frac{y - y_q}{y_j - y_q} \prod_{\substack{k_1 \leqslant s \leqslant k_2 \\ s \neq k}} \frac{z - z_s}{z_k - z_s} F_{ijk} \right], \tag{B.1}$$

where F can be temperature, species mass fractions, pressure, or any other physical properties.

Appendix C. Exact solution to one-dimensional nonscattering gray medium enclosed by black bounding surfaces

For a nonscattering gray medium enclosed by two plane-parallel black bounding surfaces that are separated by a distance of L, the theoretical solutions for the incident radiation, radiative heat flux, and radiation source term are, respectively [1],

$$G^+(\tau) = 2\pi[I_{b1}\cdot E_2(\tau) + I_{b2}\cdot E_2(\tau_L-\tau) + \int_0^\tau I_b(\tau')\cdot E_1(\tau-\tau')\,\mathrm{d}\tau' + \int_\tau^{\tau_L} I_b(\tau')\cdot E_1(\tau'-\tau)\,\mathrm{d}\tau'\Big], \tag{C.1}$$

$$q^+(\tau) = 2\pi[I_{b1}\cdot E_3(\tau) - I_{b2}\cdot E_3(\tau_L-\tau) + \int_0^\tau I_b(\tau')\cdot E_2(\tau-\tau')\,\mathrm{d}\tau' - \int_\tau^{\tau_L} I_b(\tau')\cdot E_2(\tau'-\tau)\,\mathrm{d}\tau'], \tag{C.2}$$

and

$$[\nabla\cdot\vec{q}_{\mathrm{rad}}]^+ = 4\kappa_p^+(T^+)^4 - \kappa_p^+ G^+, \tag{C.3}$$

where $E_n(x)$ is the exponential integral of order n,

$$E_n(x) = \int_1^\infty \mathrm{e}^{-xt}\frac{\mathrm{d}t}{t^n}, \quad n = 0,1,2,\ldots \tag{C.4}$$

It can be readily verified that the following recurrence relationship holds,

$$\frac{\mathrm{d}E_n}{\mathrm{d}x}(x) = -E_{n-1}(x), \quad n = 1,2,\ldots \tag{C.5}$$

For a given spatial distribution of temperature, Eqs. (C.1)–(C.3) must be numerically solved to obtain the theoretical values for G^+, q^+, and $[\nabla\cdot\vec{q}_{\mathrm{rad}}]^+$ at discrete nodal points. Since $E_1(x)$ changes dramatically near $x = 0$, direct numerical integration of the last two terms in Eq. (C.1) using regular schemes will result in significant error in G^+. To ensure sufficient accuracy, the equation is first integrated by parts to replace $E_1(x)$ by $E_2(x)$ by employing Eq. (C.5), which can then be numerically integrated by, for example, Simpson's 3/8 rule. The final expression of Eq. (C.1) is as follows:

$$\begin{aligned} G^+(\tau) = {} & 2[(T^+)^4(0)\cdot E_2(\tau) + (T^+)^4(\tau_L)\cdot E_2(\tau_L-\tau)] \\ & + 2\left[(T^+)^4(\tau)\cdot E_2(0) - (T^+)^4(0)\cdot E_2(\tau) - 4\int_0^\tau (T^+)^3(\tau')\cdot\frac{\mathrm{d}(T^+)}{\mathrm{d}x}(\tau')\cdot\frac{1}{\kappa_p^+(\tau')}\cdot E_2(\tau-\tau')\,\mathrm{d}\tau'\right] \\ & + 2\left[(T^+)^4(\tau)\cdot E_2(0) - (T^+)^4(\tau_L)\cdot E_2(\tau_L-\tau) + 4\int_\tau^{\tau_L} (T^+)^3(\tau')\cdot\frac{\mathrm{d}(T^+)}{\mathrm{d}x}(\tau')\cdot\frac{1}{\kappa_p^+(\tau')}\cdot E_2(\tau'-\tau)\,\mathrm{d}\tau'\right]. \end{aligned} \tag{C.6}$$

References

[1] M.F. Modest, Radiative Heat Transfer, second ed., Academic Press, 2003.
[2] Y. Ju, G. Masuya, P.D. Ronney, Effects of radiative emission and absorption on the propagation and extinction of premixed gas flames, Proc. Combust. Inst. 27 (1998) 2619–2626.
[3] A. Townsend, The effects of radiative transfer on turbulent flow of a stratified fluid, J. Fluid Mech. 3 (1958) 361–375.
[4] G.M. Sheved, R.A. Akmayev, Influence of radiative heat transfer on turbulence in planetary atmospheres, Atmos. Oceanic Phys. 34 (1977) 1286–1401.
[5] T.H. Song, R. Viskanta, Interaction of radiation with turbulence: application to a combustion system, J. Thermoph. Heat Transfer 3 (1987) 52–62.
[6] A. Soufiani, P. Mignon, J. Taine, Radiation–turbulence interaction in channel flows of infrared active gases, in: Proceedings of Ninth International Heat Transfer Conference, vol. 6, 1990, pp. 403–408.
[7] R.J. Hall, A. Vranos, Efficient calculations of gas radiation from turbulent flames, Intern'l. J. Heat Mass Transfer 37 (17) (1994) 2745–2750.

[8] S.R. Tieszen, On the fluid mechanics of fires, Ann. Rev. Fluid Mech. 33 (2001) 67–92.
[9] R.W. Bilger, Future progress in turbulent combustion research, Prog. Energy Combust. Sci. 26 (2000) 367–380.
[10] J.P. Gore, G.M. Faeth, Structure and spectral radiation properties of turbulent ethylene/air diffusion flames, Proc. Combust. Inst. 21 (1986) 1521–1531.
[11] M.E. Kounalakis, J.P. Gore, G.M. Faeth, Turbulence/radiation interactions in nonpremixed hydrogen/air flames, Proc. Combust. Inst. 22 (1988) 1281–1290.
[12] G. Cox, On radiant heat transfer from turbulent flames, Combust. Sci. Technol. 17 (1977) 75–78.
[13] S. Mazumder, M.F. Modest, A PDF approach to modeling turbulence–radiation interactions in nonluminous flames, Intern'l. J. Heat Mass Transfer 42 (1999) 971–991.
[14] G. Li, M.F. Modest, Investigation of turbulence–radiation interactions in reacting flows using a hybrid FV/PDF Monte Carlo method, J. Quant. Spectrosc. Radiat. Transfer 73 (2002) 461–472.
[15] P.J. Coelho, O.J. Teerling, D. Roekaerts, Spectral radiative effects and turbulence/radiation interaction in a non-luminous turbulent jet diffusion flame, Combust. Flame 133 (2003) 75–91.
[16] P.J. Coelho, Detailed numerical simulation of radiative transfer in a nonluminous turbulent jet diffusion flame, Combust. Flame 136 (2004) 481–492.
[17] L. Tessé, F. Dupoirieux, J. Taine, Monte Carlo modeling of radiative transfer in a turbulent sooty flame, Intern'l. J. Heat Mass Transfer 47 (2004) 555–572.
[18] J.-F. Ripoll, An averaged formulation of the M1 radiation model with mean absorption coefficients and presumed probability density functions for turbulent flows, J. Quant. Spectrosc. Radiat. Transfer 83 (2004) 493–517.
[19] D.C. Haworth, T.J. Poinsot, Numerical simulations of Lewis number effects in turbulent premixed flames, J. Fluid Mech. 244 (1992) 405–436.
[20] P. Moin, K. Mahesh, Direct numerical simulation: a tool in turbulence research, Annu. Rev. Fluid Mech. 30 (1998) 539–578.
[21] D. Veynante, L. Vervisch, Turbulent combustion modeling, Prog. Energy Combust. Sci. 28 (2002) 193–266.
[22] T. Poinsot, D. Veynante, Theoretical and Numerical Combustion, R.T. Edwards Inc., 2001.
[23] J.M. Hammersley, D.C. Handscomb, Monte Carlo Methods, Methuen & Co., Ltd/John Wiley & Sons, Inc., 1965.
[24] J.S. Liu, Monte Carlo Strategies in Scientific Computing, Springer, 2002.
[25] M. Baum, Etude de l'allumage et de la structure des flames turbulentes, Ph.D. thesis, Ecole Centrale de Paris, 1994.
[26] S. Lele, Compact finite difference schemes with spectral-like resolution, J. Comput. Phys. 103 (1992) 16–42.
[27] T. Poinsot, S. Lele, Boundary conditions for direct simulations of compressible viscous flows, J. Comput. Phys. 101 (1992) 104–129.
[28] C.F.J. Ridders, A new algorithm for computing a single root of a real continuous function, IEEE Trans. Circuits Syst. CAS-26 (1979) 979–980.
[29] Combustion Research Facility, Sandia National Laboratories, Intern'l. Workshop on Measurement and Computation of Turbulent Nonpremixed Flames, (http://www.ca.sandia.gov/TNF/radiation.html, 2002).
[30] N.C. Barford, Experimental Measurements: Precision, Error and Truth, Addison-Wesley, London, 1967.
[31] Y. Wu, D.C. Haworth, M.F. Modest, B. Cuenot, Direct numerical simulation of turbulence/radiation interaction in premixed combustion systems, Proc. Combust. Inst. 30 (2005) 639–646.
[32] K.V. Deshmukh, M.F. Modest, D.C. Haworth, Direct numerical simulation of turbulence radiation interactions in a statistically one-dimensional nonpremixed system, in: Proceedings of Eurotherm78 – Computational Thermal Radiation in Participating Media II, 2006.
[33] K.V. Deshmukh, D.C. Haworth, M.F. Modest, Direct numerical simulation of turbulence–radiation interactions in nonpremixed combustion systems, Proc. Combust. Inst. 31 (2007) in press.
[34] C. Jiménez, B. Cuenot, T. Poinsot, D. Haworth, Numerical simulation and modeling for lean stratified propane-air flames, Combust. Flame 128 (2002) 1–21.